catalysts

MDPI

Article

Reconstruction of Electronic Structure of MOF-525 via Metalloporphyrin for Enhanced Photoelectro-Fenton Process

Chenhui Qi [1], Shuaipeng Han [1], Jialiang Lin [1], Jianhua Cheng [1,2,*], Kesi Du [1,*], Yongyou Hu [1] and Yuancai Chen [1]

[1] Guangdong Provincial Key Laboratory of Solid Wastes Pollution Control and Recycling, College of Environment and Energy, South China University of Technology, Guangzhou 510006, China; qichenhui0414@163.com (C.Q.); alivesphan@163.com (S.H.); ljl2ax@hotmail.com (J.L.); ppyyhu@scut.edu.cn (Y.H.); chenyc@scut.edu.cn (Y.C.)

[2] South China Institute of Collaborative Innovation, Dongguan 523808, China

* Correspondence: jhcheng@scut.edu.cn (J.C.); dukesi@scut.edu.cn (K.D.)

Abstract: Photoelectro-Fenton (PEF) process can continuously promote the occurrence of Fenton reaction and the generation of active species, which is an advanced oxidation technology for pollutant degradation. However, the lack of bifunctional catalysts restricts the development of PEF technology. In this study, the electronic rearrangement MOF-525 modified by metalloporphyrin (named MOF-525-Fe/Zr) was prepared, to load on the carbon felt as a novel cathode catalyst, which is used in PEF process. A series of characterization and photoelectric chemical properties tests combined with DFT calculation showed that the modification of MOF-525 could not only have the large specific surface area and multistage pore structure but also co-stimulate the metal-to-ligand charge transfer (MLCT) and ligand-to-cluster charge transfer (LCCT) by photoelectric synergy. These charge transitions provide periodic electron donor-acceptor conduction paths in MOF-525-Fe/Zr, which can improve the active species formation and transfer efficiency. Owing to their favorable pore and electronic structure as well as stability, MOF-525-Fe/Zr shows great promise for the application in the catalytic process of PEF. Sulfamethoxazole (SMX) degradation was enhanced by MOF-525-Fe/Zr with the TOC removal rate above 75% both in river water and tap water. Finally, the reasonable pathway of PEF catalytic degradation of SMX was proposed by HPLC-MS analysis. In conclusion, this study provides a new idea for reconstructing the electronic structure of MOFs catalyst and broadening the practical application of PEF technology.

Keywords: photoelectro-Fenton; MOF-525; metal-to-ligand charge transfer; ligand-to-cluster charge transfer; sulfamethoxazole

Citation: Qi, C.; Han, S.; Lin, J.; Cheng, J.; Du, K.; Hu, Y.; Chen, Y. Reconstruction of Electronic Structure of MOF-525 via Metalloporphyrin for Enhanced Photoelectro-Fenton Process. *Catalysts* **2022**, *12*, 671. https://doi.org/10.3390/catal12060671

Academic Editor: Marta Pazos Currás

Received: 16 May 2022
Accepted: 14 June 2022
Published: 19 June 2022

1. Introduction

The outbreak of coronavirus in 2019 has driven the demand for convenient and efficient wastewater treatment technologies, including Fenton, Fenton-like processes [1]. Fenton reaction refers to the redox reaction in which the intermediate active species hydroxyl radical (•OH) was rapidly generated by hydrogen peroxide (H_2O_2) and ferrous ion (Fe^{2+}) in an acidic solution. The specific reaction formula is shown in Equation (1) [2]. •OH with strong oxidability easily oxidizes target pollutants and thus mineralizes and degrades them (Equation (2)) [2]. However, there are secondary pollution of iron sludge and a high cost of H_2O_2 (Equation (3)) [3,4]. As a typical Fenton-like technology, photoelectro-Fenton (PEF) can effectively solve these problems. In the PEF process, ultraviolet (UVA and UVC), solar or visible light sources are introduced to the basis of the original electric Fenton device. PEF combines the advantages of the electro-Fenton (EF) (producing the situ H_2O_2, (Equation (4)) [5] and photo-Fenton (PF) (catalyzing formation of Fe^{3+}/Fe^{2+} cycle), further inducing the •OH formation and enhancing the pollutant degradation efficiency of the Fenton reaction (Equations (5)–(7)) [6,7]. PEF process provides a photoelectric

co-catalytic process with high efficiency, breaking through the limitations of a single Fenton-like process [8,9]. PEF technology has been successfully used in wastewater treatment to further remove no-biodegradable organic pollutants, such as benzabate, ciprofloxacin, rhodamine B (RhB), and dimethyl phthalate (DMP) [10–13]. These results indicate that PEF process can achieve deep removal of organic pollutants because of abundant active species.

$$H_2O_2 + Fe^{2+} + H^+ \rightarrow Fe^{3+} + \bullet OH \quad (1)$$

$$\bullet OH + RH \rightarrow R + H_2O \quad (2)$$

$$3H_2O + Fe^{3+} \leftrightarrow Fe(OH)_3 + 3H^+ \quad (3)$$

$$O_2 + 2H^+ + 2e^- \rightarrow H_2O_2 \quad (4)$$

$$Fe^{3+} + hv \rightarrow Fe^{2+} \quad (5)$$

$$H_2O + Fe^{3+} \leftrightarrow Fe(OH)^{2+} + H^+ \quad (6)$$

$$Fe(OH)^{2+} + hv \rightarrow Fe^{2+} + \bullet OH \quad (7)$$

Catalysts that catalyze the formation of active species play an important role in the PEF process. Its photoelectric catalysis performance directly determines the generation and mass transfer efficiency of active species and then affects the oxidative degradation capacity of PEF reaction [14]. Metal-organic frameworks (MOFs) are a class of spatially ordered crystalline materials, usually formed by the coordination of different metal ions or metal cluster secondary building units (SBUs) with organic ligands [15]. It has the advantages of high specific surface area, open metal sites, and adjustability. By designing and selecting a variety of metal clusters and ligand types, the framework structure and chemical composition of MOFs can be regulated, and the potential photoelectric chemical activity of MOFs materials can be fully explored [16]. In recent years, diverse MOFs and their derivatives have been synthesized and extensively used to catalyze the degradation of pollutants in PF and EF process [17,18]. In contrast, the application of MOFs in PEF process has been rarely reported. Ye et al. reported the Fe-based 2D MOF prepared with 2,2′-bipyridine-5,5′-dicarboxylate (bpydc) as an organic linker, as highly active heterogeneous catalyst for PEF treatment. However, it is not reusable and the degradation effect decreases obviously after three cycles [12]. Zhao et al. directly combined MOF (2Fe/Co) with carbon aerogel (CA) as a cathode to fully stimulate the electrocatalytic and photocatalytic activity of the MOF in PEF process. However, MOFs modified in this way also have poor stability, which is reflected in the leaching rate of Fe and Co ions increasing with the increase of reaction times [10]. Within this context, this study is to reconstruct a new MOF-modified cathode, which has both structural stability and PEF catalytic activity and has the ability to be applied to the degradation of actual water pollutants. MOF-525, a Zr-based MOF, is formed by the link of meso-tetracarboxyphenyl porphyrin (H_2TCPP) and Zr-oxo SBUs. Some research suggested that MOF-525 has an ftw topology and strong stability, where each Zr_6 cluster contain 12 liners providing a large number of redox sites and strong coordination between Zr^{IV} nodes and surface carboxyl groups on the basis of the soft-hard acid-base principle [19,20]. Meanwhile, the highly conjugated porphyrin rings with 26 π electrons were used as organic linkers to solve the problem of light capture. However, due to the electrical insulation or low conductivity of MOF, the efficient charge transfer within the frame is one of the major challenges that restrict the performance of MOF-based photoelectric catalysts. At present, the main research direction is to solve the problem of impeded charge transfer of organic ligands through pyrolysis carbonization of MOF [21]. However, to improve the electrical conductivity and retain the light absorption of MOFs organic ligands, this study designed modified organic ligands which build an electron donor-acceptor (D-A) system in the entire MOF framework structure and promote the long-range movement of charge carriers in the bulk crystal domain.

Due to the fact that, in the porphyrin pyrrole ring, the H atom is easily replaced by metal ions and four heterocyclic nitrogen atoms can be used as free metal-chelating

sites, Fe catalyzed active metal sites can be introduced to modify porphyrin ligands in MOFs. In addition to their natural conductive properties, iron-based chromophores are useful for photoinduced electron transfer under external stimuli, such as voltage and light, including solar energy conversion and catalysis [22]. Wang et al. prepared MOF-525 (Cu) series by mixing a Cu-embedded metalloporphyrin ligand with $ZrOCl_2 \cdot 8H_2O$ and acetic acid. The test results showed that MOF-525(Cu) exhibited excellent charge and discharge rate and cycling performance as the main body of lithium-sulfur batteries [23]. Lee et al. introduced unsaturated monatomic Co into MOF-525 through the synthesis of Co-TCPP, which achieved efficient and selective capture and photo-reduction of CO_2 under photocatalytic conditions [24].

Based on the previous work, MOF-525-Fe/Zr can be synthesized by introducing iron porphyrins (Fe-TCPP) into the MOF-525 frame structure in this study, to change the original MOF electronic structure and construct the D-A periodic charge transfer paths within the framework. MOF-525-Fe/Zr was coated on carbon felt (CF) to form a modified cathode, and its reuse in PEF system was realized. We expect that this work will provide some valuable information for the design of high-performance PEF catalysts. Consumption of stimulants and personal care products (PPCPs) has risen sharply amid the current COVID-19 pandemic outbreak [25]. Sulfamethoxazole (SMX), as the most frequently detected PPCPs emerging pollutants in water, was selected as the target pollutant in this degradation process because of its biological toxicity and environmental risk [26,27]. The photoelectric catalysis performance of MOF-525-Fe/Zr-modified cathode was evaluated by analyzing the degradation efficiency of SMX in PEF process.

2. Results and Discussion

2.1. Composition and Structural Characterization of Catalysts

The morphology of the catalyst and its modified cathode were observed by SEM images. MOF-525-Fe/Zr still retains the cubic morphology of MOF-525, indicating that the modification method of the pre-metallized porphyrin ligand can retain the crystal structure of the original MOF (Figure 1a) [28]. Meanwhile, the comparison between SEM images of pure CF and MOF-525-Fe/Zr-modified CF (named MOF-525-Fe/Zr) clearly shows that the catalyst can be uniformly coated on the surface of CF, which proves that MOF-525-Fe/Zr can be successfully loaded on the CF to form modified cathode (Figure 1b,c). The load of continuous nucleated MOF-525-Fe/Zr nanoparticles on CF would increase the electrical conductivity of nanocomposites by reducing the grain boundaries and contact resistance [29].

To go a step further, using HAADF-TEM with EDX is capable of acquiring the elemental information of a single MOF-525-Fe/Zr crystal cell. EDX elemental mapping images shows the clearly identified atomically uniform dispersed C, N, O, Fe, Zr atoms in the HAADF-STEM images of the MOF-525-Fe/Zr catalyst (Figure 1d,e) [30]. With further quantification analysis in the regions of individual atoms demonstrated, there is N around each Fe atom and the atomic ratio of N:Fe:Zr:C:O is approximately 4:1:4:240:30, thus providing the compositional evidence for the Zr-oxo SBUs coordination FeN_4 porphyrinic structures (Table 1). Related studies show that Fe-TCPP with FeN_4 structure formed by the coordination of central metal ions has stronger ORR performance due to its own D-A structure [31].

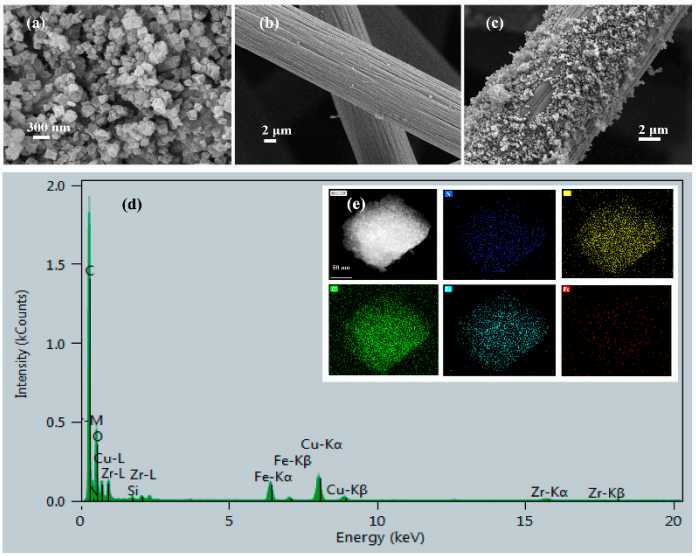

Figure 1. SEM images of (**a**) MOF-525-Fe/Zr (**b**) CF (**c**) MOF-525-Fe/Zr@CF; STEM-EDX scanning of MOF-525-Fe/Zr of (**d**) its normalized N, O, C, Fe, and Zr signals and (**e**) its composition maps of N, O, C, Fe, and Zr elements.

Table 1. Analysis of element composition spectrum (EDX) of single MOF-525-Fe/Zr crystal cell.

Element	Atomic Fraction (%)	Measurement Error (%)	Mass Fraction (%)
C	86.23	3.09	74.66
N	1.41	0.25	1.42
O	10.41	2.74	12.01
Fe	0.36	1.28	1.45
Zr	1.59	0.68	10.41

N_2 adsorption isotherms of MOF-525 and MOF-525-Fe/Zr catalysts are shown in Figure 1. The specific surface area of MOF-525 and MOF-525-Fe/Zr can be calculated by Brunauer–Emmett–Teller (BET) method to be 625.32 m^2/g and 428.22 m^2/g, respectively. According to the classification of IUPAC, N_2 adsorption isotherm shows the hysteresis loop, so MOF-525 and MOF-525-Fe/Zr belong to the characteristic type IV adsorption curve. This further indicates that the modification of MOF-525 by pre-metallized porphyrin can retain the adsorption properties of MOF-525. The hysteresis curves indicate that capillary condensation occurs in the adsorption pores, suggesting the existence of micropores and mesoporous pores in both skeleton structures [32].

Furthermore, the pore size distribution of hollow and large pores was analyzed based on Barrett–Jouner–Halenda (BJH) method, and the pore size distribution of micropores was analyzed based on Horvath–Kawazoe (HK) method [33,34]. The calculation results are shown in Table 2. The pore volume and pore size of MOF-525 and MOF-525-Fe/Zr are 0.367 cm^3/g and 2.347 nm, and 0.371 cm^3/g and 3.682 nm, respectively. Combined with Figure 2b, it can be inferred that MOF-525 is mainly a microporous structure, while MOF-525-Fe/Zr has a wider distribution range of pore size and a multistage pore structure of the micropore-mesopore level. The area and volume of pores in the range of 0–120 nm are obtained by further analysis of adsorption isotherm curve with BJH method. As can be seen from Figure 2c,d, the pore area of MOF-525 is mainly provided by mesopore, accounting for 65.33% of the total pore volume. In the calculation of the cumulative contribution ratio of MOF-525-Fe/Zr pore area, the proportion of mesopore increases to 85.01%. The significant difference in proportion indicates that the increase in the number of mesopores in MOF-525-Fe/Zr greatly affects the pore area [35]. But the BET calculation of specific surface area is mainly based on the micropores, which results in a slight decrease of MOF-

525-Fe/Zr specific surface area compared with MOF-525. Meanwhile, it can be seen that the multistage pore structure further enlarges the pore volume of MOF-525-Fe/Zr [36,37].

Table 2. Specific surface area and pore structure parameters of MOF-525 and MOF-525-Fe/Zr.

Catalyst Type	Specific Surface Area (m^2/g)	Total Pore Volume (cm^3/g)	Average Pore Size (nm)
MOF-525	625.32	0.367	2.347
MOF-525-Fe/Zr	428.22	0.371	3.682

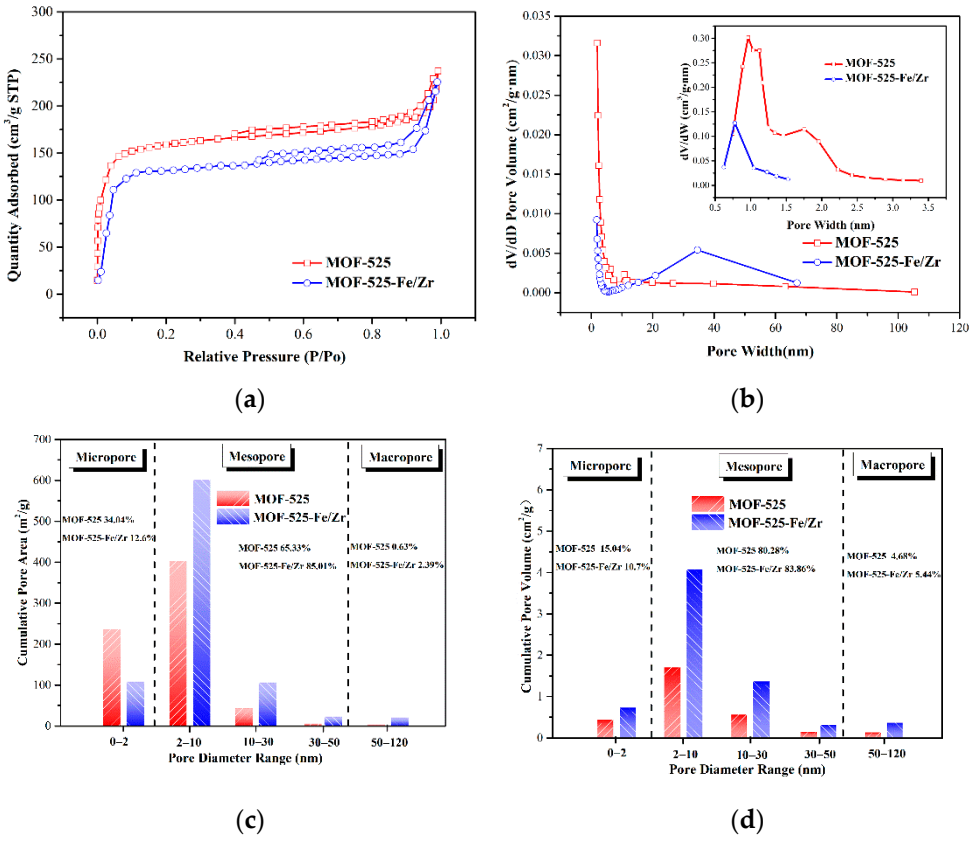

Figure 2. (**a**) N_2 adsorption isotherm; (**b**) pore size distribution; (**c**) incremental pore area; and (**d**) incremental pore volume of MOF-525 and MOF-525-Fe/Zr.

These results indicate that the coordination of iron ion and TCPP changes the original pore structure of MOF-525, resulting in the formation of large defect space on the surface and inside of MOF-525 [38,39]. The assembly of Fe-TCPP in MOF-525 three-dimensional network leads to the combined expansion of micropores, which effectively inhibits the molecular accumulation. The pore volume of MOF-525-Fe/Zr is larger than that of MOF-525, which can support the rapid diffusion and transportation of active species and reactants. MOF-525-Fe/Zr can combine the high specific surface area with the characteristics of a multi-pore structure, thus providing more adsorption and reaction active sites and improving electronic structure and Fenton reaction catalytic activity [40,41].

Due to the sensitivity of molecular vibration to molecular structure and electronic properties, Raman spectroscopy is one of the characterization methods to explore the chemical bond information and electronic structure information changes in MOF [42]. The high-frequency region (800–2000 cm^{-1}) reflects the vibration mode of the organic skeleton, and the low-frequency region (200–700 cm^{-1}) reflects the vibration mode of the zirconium oxygen cluster and the axial iron ligand bond [43]. The similarity between MOF-52-Fe/Zr and MOF-525 vibration peaks (Figure 3) indicates that the symmetry of the characteristic structure of MOF-525 has not been changed after the metallization of porphyrin. But at

the same time, it can be seen that the vibration peak intensity of MOF-525-Fe/Zr is weaker than that of MOF-525 on the whole, indicating that the conjugation degree of the organic skeleton part of MOF-525-Fe/Zr increases as well as the degree of charge delocalization [44]. The peaks at 1453 and 1493 cm^{-1} in MOF-525-Fe/Zr spectra are assigned to the vibration duality of C=O, indicating the enhanced symmetry of the inward and outward tensile vibration of the carboxylic acid group, which can also prove the above viewpoint [27]. Moreover, this π-conjugated structure in carboxylic acid groups also provides a platform to facilitate electron transfer between them in the process of catalytic conversion [45]. In addition, at the high vibration frequency region of MOF-525-Fe/Zr spectrum, the wavelet number shift of the C-N group (817 cm^{-1}), C=C group (1326 cm^{-1})in the pyrrole ring, and C=C group (1362 cm^{-1}), C-C group in the benzene ring (1453 cm^{-1}) relative to MOF-525 spectra also provides evidence for the heterogeneity of charge transfer in the porphyrin ring [46]. The disappearance of the N-H bond in the porphyrin ring (1762 cm^{-1}) and the existence of the Fe-N bond (413 cm^{-1}) further suggest the insertion of Fe ions into the central nucleus of the porphyrin, which leads to the change of the electronic structure in the MOF-525 [47]. The shift of O-Zr-O symmetric vibration peak at 321 and 426 cm^{-1} in MOF-525-Fe/Zr spectra demonstrates that the coordination of Fe-TCPP and Zr-oxo SBUs changes the electron density of the primary metal site [48].

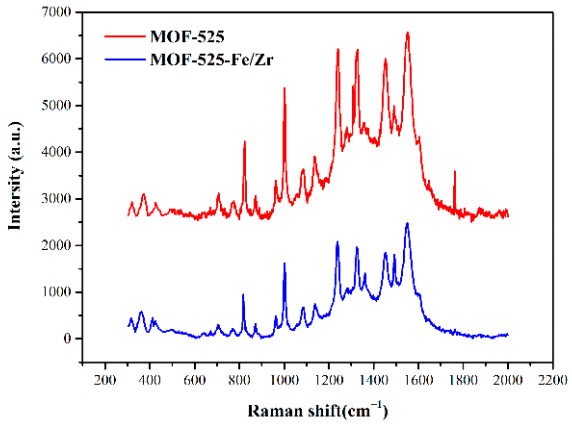

Figure 3. Raman spectra of MOF-525 and MOF-525-Fe/Zr.

2.2. Analysis of Photoelectric Properties

Accurate and efficient assessment inactivity for electrocatalytic oxygen reduction (ORR) is critical for the development of PEF catalysts [49]. The ORR kinetics mechanism can be revealed using linear sweep voltammetry (LSV) test electrode polarization curve and the Tafel slope b fitted by the Tafel formula (Equation (8)) [50]. As shown in Figure 4a, the Tafel slope of MOF-525-Fe/Zr is 42 mV/dec, which is significantly lower than that of MOF-525 (74 mV/dec) as well as some commercial ORR electrocatalysts, such as Pt/C (86 mV/dec) and IrO_2 (120 mV/dec) and the Pt/Pd/Co-NC (74 mV/dec) [51,52]. The comparison results show that MOF-525-Fe/Zr has lower ORR resistance and higher charge transfer rate, which can efficiently reduce O_2 to produce an active oxidant [53]. This may be because the MLCT transition in Fe-TCPP is excited by electrochemical polarization. MLCT enables electrons to be excited from the metal local orbital to the vacancy ligand local orbital, reducing the mass transfer resistance caused by the organic ligand and enhancing the electrocatalytic activity of MOF [54].

$$\eta = a + blog|j| \quad (8)$$

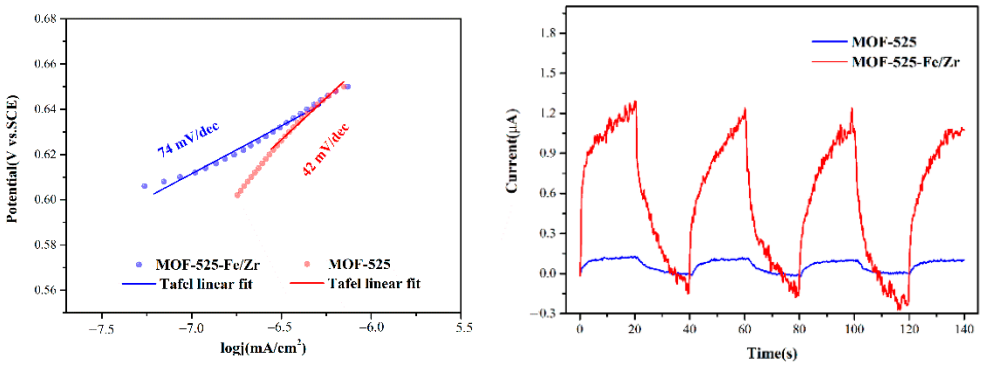

Figure 4. (**a**) Tafel slope and (**b**) transient photocurrent response of MOF-525 and MOF-525-Fe/Zr.

In order to further study the photoelectric signal response capability of PEF catalyst, MOF-525 and MOF-525-Fe/Zr were tested for transient photocurrent response [55]. As shown in Figure 4b, both catalyst electrodes exhibit transient and stable photocurrent responses each time ultraviolet light is irradiated. When the irradiation is interrupted, the photocurrent quickly drops to zero, and when the lamp is turned on again, the photocurrent immediately returns to a constant value. It can be concluded that the two catalysts have obvious "light on and light off" periodic photocurrent [56]. The maximum photocurrent of MOF-525-Fe/Zr (1.29 μA), is about ten times larger than that of MOF-525 (0.128 μA). This is related to the strong photosensitivity of the newly matched molecular orbital between Zr-oxo SBUs and Fe-TCPP π conjugated domain. The UV light can co-stimulate the LCCT and MLCT transitions in MOF-525-Fe/Zr, which further improves the migration rate of photoelectrons, inhibiting the recombination of photoelectron-hole pairs. LCCT and MLCT effectively reduce the charge transfer resistance, and improve the carrier density and optical stability [57,58].

2.3. Density Functional Theory Calculations

To understand the electronic structure, optical properties, and charge transfer mechanism of MOF-525 and MOF-525-Fe/Zr, the forward orbital of TCPP and Fe-TCPP transition was calculated by density functional theory (DFT) simulation [59]. The results are presented on the left side of Figure 5. It is found that the ground state of TCPP is a singlet state, while the ground state of Fe-TCPP process is a triplet state with the increase of electron density. In spin-unrestricted DFT calculations performed for triplet states, α and β electrons occupy different spatial orbitals, so it makes sense to compare the relative energies of the lowest triplet states [60]. The highest energy level orbital HOMO (π) on the TCPP segment is located between the pyrrole ring nitrogen and the adaptive front molecular orbital (FMO), while the lowest energy level orbital LUMO (π *) is located on the acceptor group benzene ring. Therefore, DFT calculated that TCPP has HOMO→LUMO internal charge transfer (ILCT) transitions at lower energy absorption bands [61]. However, when the pyrrole donor site further binds with iron ion, HOMO and LUMO are delocalized due to intramolecular charge separation. The HOMO electron density distribution is significantly biased toward the central Fe atom, and the lowest energy excitation state changes from (π→π *) ILCT to (d→π *) triplet ^{3}MLCT, and the light absorption band is redshifted [62]. Compared with TCPP, the HOMO-LUMO bandgap of the Fe-TCPP ground state changes from −2.65 eV to −2.51 eV, which is also attributed to the MLCT transition in the metalloporphyrin. The narrowing of the bandgap of MOF-525-Fe/Zr leads to the narrowing of the band gap between the valence band and the conduction band, which indicates that the conjugation degree of π electrons is improved.

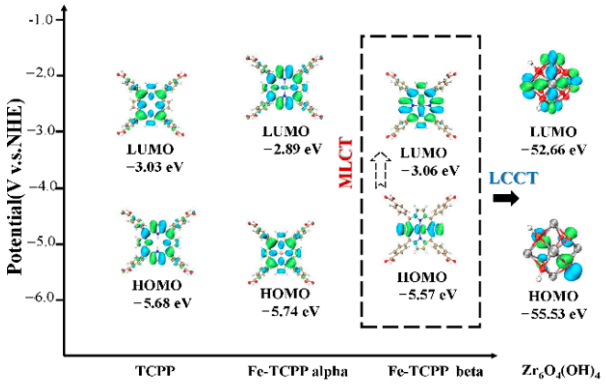

Figure 5. Distribution of orbital energy of TCPP, Fe-TCPP, and $Zr_6O_4(OH)_4$.

The front-line orbital diagram of $Zr_6O_4(OH)_4$ (Zr-oxo SBUs) is shown in Figure 4. As can be seen from the calculated orbital energy potential, the LUMO level of Zr-oxo SBUs is much lower than that of Fe-TCPP, so the low energy transition from HOMO of Fe-TCPP ligand to LUMO of Zr-oxo SBUs tends to occur. This well supports the theoretical feasibility of LCCT excitation in MOF-525-Fe/Zr [63]. The HOMO electron density on $Zr_6O_4(OH)_4$ mainly comes from the O 2p orbital of the oxygen ligand, while the Zr 4d orbital in the Zr-O nucleus dominates in the higher LUMO. The results show that the HOMO→ LUMO transition on $Zr_6O_4(OH)_4$ ascribed to the O 2p→ Zr 4d charge transfer, which further corresponds to π (Fe-TCPP ligand)→ π * (Zr-oxo SBUs) orbital LCCT transition [58]. Therefore, DFT calculation proves that the D-A electron conduction path can be reconstructed in MOF-525 through cooperative excitation of MLCT and LCCT to improve electron separation and transmission efficiency.

2.4. Catalytic Degradation of SMX in PEF Process

2.4.1. Analysis of Degradation Effect and Mechanism

Taking MOF-525(Zr) as the matrix and referring to the controllable design scheme of tunable electronic structure within the metal-organic framework summarized in the study of Chen L et al. [64], the preparation methods of different Fe-modified MOF catalysts were compared and designed. Then the modified cathodes with different MOF catalysts were used to degrade SMX in PEF system. Applying "Ship-in-bottle strategy", mix the synthesized MOF-525 and the precursor $FeSO_4$ up to obtain the metallized Fe-MOF-525 by solvothermal method, which was coated on the surface of carbon felt to obtain the modified cathode named Fe-MOF-525@CF; adopting the "Bottle-around-ship" strategy, the synthesized Fe_3O_4 was mixed with MOF-525 precursor benzoic acid, $ZrOCl_2{\cdot}8H_2O$, and TCPP to obtain the coating material MOF-525@Fe_3O_4 by solvothermal method, which was coated on the surface of carbon felt to obtain the modified cathode named MOF-525-Fe_3O_4@CF.

The photoelectron catalysis performance of five different materials is shown in Figure 6a. It can be concluded that in the PEF process, MOF-525-Fe/Zr prepared by pre-modified metal porphyrin exhibited the best degradation performance, with an SMX removal rate of 97.3%, followed by MOF-525-Fe_3O_4@CF, which has a slightly lower SMX removal rate of 70%. This due to the post-assembly synthesis MOF-525-Fe_3O_4@CF only can control the growth of MOFs but fail to achieve further charge transfer beyond the interfacial energy barrier. The degradation effect of Fe-MOF-525@CF prepared by the post-modification method exhibited not much difference from that of pure MOF-525 material and common CF, both showing inferior performance with a degradation rate lower than 50%. The difference in diffusion resistance between the outer and inner surfaces of the MOF electronic structure may account for the different catalytic performance, and the addition of metal ions after the skeleton assembly inevitably leads to the agglomeration of metal ions on the outer surface of the MOF crystal, resulting in random and unpredictable

charge transition and low catalyst activity. Ordinary CF has a degradation rate of 36.6% for SMX because it has a good adsorption performance and part of SMX is removed by electric adsorption. The fact that the degradation rate of SMX increased after MOF-525 was coated on CF, indicates the weak catalytic activity of MOF-525. This also manifested that MOF-525-Fe/Zr catalyst prepared by pre-modification of metalloporphyrin can achieve effective coordination of iron ions. The new electronic structure constructed by this method is most favorable to catalyze the degradation of SMX in PEF process.

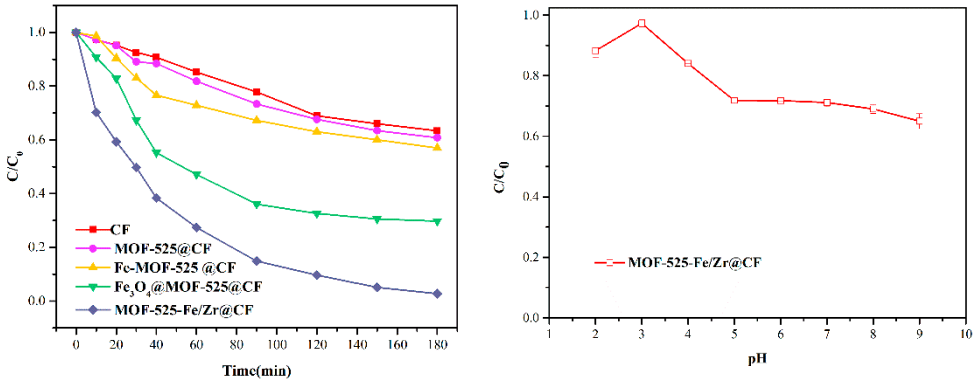

Figure 6. Comparison of SMX degradation efficiency of (**a**) different catalyst-modified cathodes, (**b**) different pH values in the PEF process.

In addition to the influence of catalyst preparation, the influence of environmental factors on the photoelectric performance of catalyst cannot be ignored. PEF process is very sensitive to the water pH; it is necessary to determine the effect of initial pH on the SMX degradation efficiencies. Better adaptability to pH change of MOF-525-Fe/Zr@CF can be observed in the PEF process for degradation of SMX [65]. At pH = 3.0, 93.7% of SMX was degraded within 180 min, while the degradation efficiency of SMX remained above 70% with the change of pH from 2.0 to 8.0 (Figure 6b). Meanwhile, MOF-525-Fe/Zr has a higher degradation efficiency for acidic water in PEF process correspondingly, and the overall degradation efficiency increases and then decreases with the increase of pH. This can be attributed to the fact that when MOF-525-Fe/Zr is suspended in an alkaline solution, the carboxylic acid groups (connector between Zr-oxo SBUs and Fe-TCPP) can be partially polarized [45].

To further investigate the efficiency of MOF-525-Fe/Zr@CF-catalyzed PEF reaction to degradation SMX in practical applications, deionized water, tap water, and river water were used as the sample solution. Before the reaction the sample solutions were filtered through a 0.45 μm microporous membrane and the initial pH was adjusted to 3.0, so as to compare the degradation efficiency of the sample solutions more accurately. With MOF-525-Fe/Zr@CF as the cathode and platinum sheet as the anode, an evaluation experiment was carried out. According to the experimental results of the catalytic PEF reaction in Figure 7a, the degradation rates of the MOF-525-Fe/Zr-modified cathode toward SMX in deionized water, tap water, and river water are 97.3%, 90.2%, and 82.0%, respectively. The reason for the decrease in degradation rate is that other organic pollutants in tap water and river water would react with oxidative substances,(such as active free radicals in the process) acting as competitors of SMX. We further tested the TOC value of each reaction solution sample, and the results are shown in Figure 7b and Table 3. The results further confirmed that the initial TOC values of tap water and river water were higher, demonstrating the concentration of organic pollutants was higher. Despite the interference of various organic pollutants, it can be seen in the above figure that with the prolongation of the reaction time, the SMX degradation efficiency of MOF-525-Fe/Zr-modified cathode continued to increase, and after 180 min, the TOC removal rates of the three water samples were more than 75%.

Moreover, MOF-525-Fe/Zr-modified cathode significantly improves the mineralization rate of SMX compared with MOF-like catalysts proposed in previous studies (Table 3) [66–74].

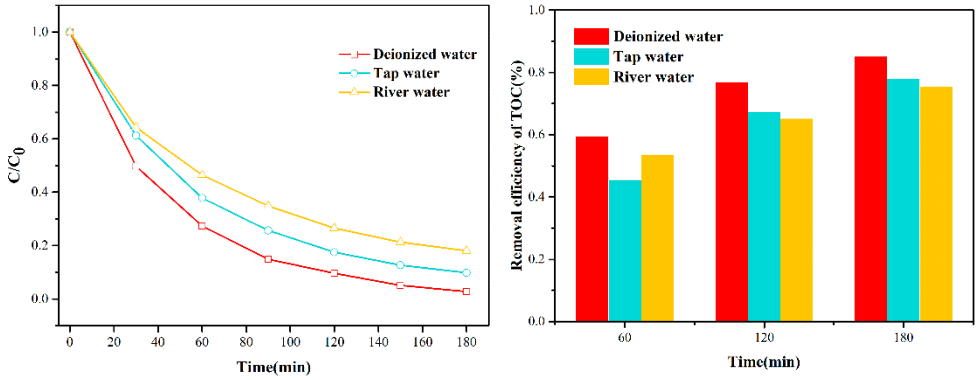

(**a**) (**b**)

Figure 7. (**a**) Effect of MOF-525-Fe/Zr@CF degradation of SMX in different wastewater in PEF system; (**b**) TOC degradation efficiency diagram.

Table 3. Comparison of SMX degradation efficiency of related catalysts.

Catalyst Type	Technology	Time	Initial Concentration of SMX (mg/L)	SMX Degradation Rate (%)	TOC Mineralization Rate (%)	Ref.
UiO-66-NH_2/Ag_3PO_4 MOF	Adsorption	120 min	50	35	-	[66]
Ni-MOF-74	MFCs	2 days	10	61	-	[69]
MOF derived Fe@C	PMS	360 min	10	100	76.2	[70]
Activated MIL-53(Fe)	PF	120 min	0.2	90–96	30	[72]
MOF-derived N-doped ZnO carbon skeleton@hierarchical Bi_2MoO_6	PF	120 min	10	72	-	[73]
Fe_3S_4 derived from MIL-100(Fe)	PF	40 min	5	100	41	[71]
CuCo–O@CNTs/NF electrode	EF	60 min	10	100	38.5	[74]
CNT/r-FeOOH	Bio-EF	48 h	25	56.28	40.21	[68]
Activated carbon fiber (ACF) cathode	PEF	6 h	300	100	80	[67]
MOF-525-Fe/Zr@CF	PEF	180 min	10	97.3	85	This study

In order to verify the catalytic stability and reuse the MOF-525-Fe/Zr@CF in PEF process, repetitive degradation was performed. After each degradation test, the MOF-525-Fe/Zr@CF was washed with acetone, retrieved, and dried naturally for further reutilization. Under the same experimental conditions of five cycles, the SMX degradation rate of MOF-525-Fe/Zr@CF remained above 95% and only a negligible efficiency reduction (1%) was observed after the fifth run in PEF process (Figure 8). The leaching concentration test results of metallic elements (Fe and Zr ions) from MOF-525-Fe/Zr@CF cathode after each cycle experiment are also shown in Figure 8. It revealed that the concentrations of leaching Fe and Zr both decrease with the number of cycles resulting in a maximum value of 0.72 mg/L and 0.31 mg/L respectively, which is far lower than the permitted amount of drinking water advised by the World Health Organization (2 mg/L) [75].

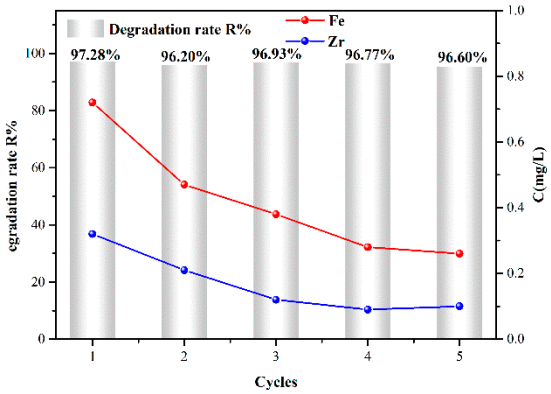

Figure 8. The leaching concentration of iron zirconium ion and degradation efficiency of SMX in five cycles.

As is obvious from these results, MOF-525-Fe/Zr@CF presented significant chemical stability and could overcome the poor reusability of most MOF and PEF catalysts [76,77]. It is because the Zr-oxo SBUs with high connectivity and high charge density form very strong Zr−O bonds and the porphyrin ring binds to Fe(II) ion to form desirable reticular framework, thus minimizing its hydrolysis [78]. These findings indicate the MOF-525-Fe/Zr-modified cathode has good water stability and high reusability in PEF reaction system, is environmentally friendly, and has strong practical application potential.

In order to study the generation and transformation mechanism of the main active radical •OH during the catalytic PEF process of MOF-525-Fe/Zr@CF, the concentrations of H_2O_2 and •OH under the same conditions were further evaluated. The measurement data showed that using the catalyst in the PEF process, the concentration of H_2O_2 reached 12.95 $mg{\cdot}L^{-1}$ within 180 min, and the yield of •OH reached 1.03 mM. Compared with other PEF catalysts, it has obvious advantages in H_2O_2 accumulation and •OH conversion (Table 4) [79–82].

Table 4. The production of H_2O_2 and •OH in catalytic Fenton-like systems is summarized and compared.

Cathode	Anode	Technology	Time (Min)	Pollutants	H_2O_2 (Max) ($mg{\cdot}L^{-1}$)	•OH (μM)	Ref.
MOF-525-Fe/Zr@CF	Pt	PEF	180	SMX	12.95	1030	This study
$Fe@Fe_2O_3$/CF	TiO_2	PEF	120	Coal gasification wastewater	1.43	-	[81]
ACF felt	RuO_2/Ti mesh	PEF	120	SMX	0.023	-	[79]
CoSxPy/ MWCNTs air-diffusion electrode	RuO2-based anode	PEF	360	bronopol	0.088	-	[82]
Fe_3O_4/GDE	Pt	EF	60	Tetracycline	Almost no	34.5	[80]
Mn/Fe@PC-CP	Pt	EF	120	Triclosan	14.5	130	[32]

Thus, the mechanism of MOF-525-Fe/Zr-modified cathode-catalyzed PEF degradation is tentatively proposed. First, the light source and the power supply in the PEF process can accelerate the carrier transport process by synergistically stimulating the MLCT and LCCT transitions on MOF-525-Fe/Zr surface. The carriers including photogenerated electrons (e_{CB}^-), holes (h_{VB}^+), and cathode electrons (e^-) further catalyze the occurrence of a series of redox reactions centered on Fenton reactions (such as ORR and surface metal redox reactions). Second, the active species (•OH, h^+ and $•O_2^-$) continuously produced by redox

reactions can completely degrade SMX and convert it into CO_2 and H_2O [83]. The specific reaction process and mechanism are shown in Figure 9.

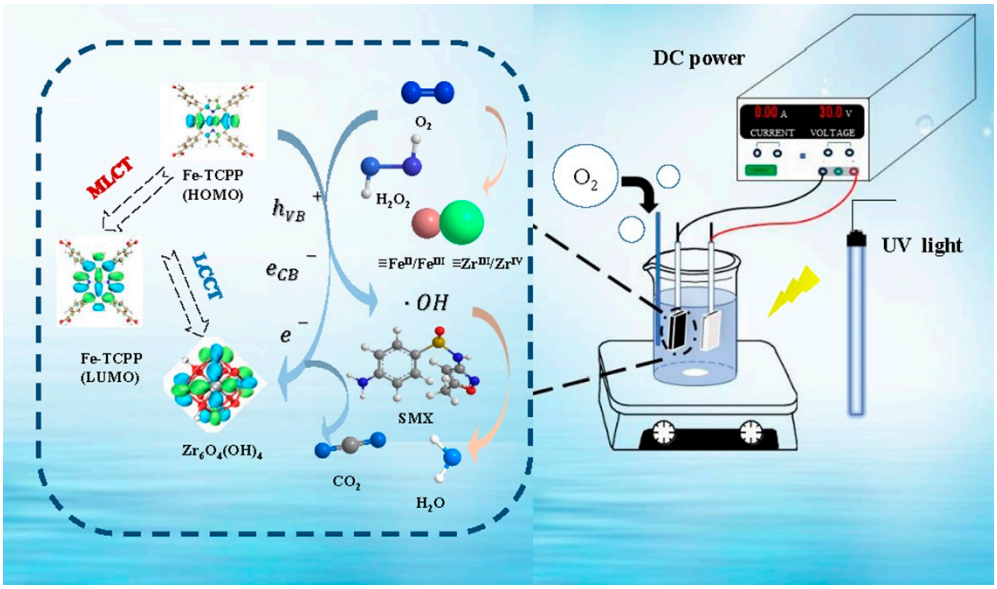

Figure 9. Mechanism diagram of SMX degradation in PEF process.

2.4.2. SMX Degradation Pathway Analysis

According to the experimental results in Section 2.4.1, after 180 min reaction, the SMX degradation rate and TOC degradation rate of MOF-525-Fe/Zr-modified cathode reached 97.3% and 85%, respectively, not 100%. This indicates the formation of intermediates in the degradation process. The intermediates of SMX degradation in MOF-525-Fe/Zr catalyzed PEF process were determined and analyzed by HPLC-MS. The spectrogram obtained was compared with the instrument database, and the corresponding SMX degradation pathway was obtained as shown in Figure 10, and the mass spectrogram of intermediate compounds is shown in Figure 11.

Three main conversion pathways (A, B, and C) of SMX are proposed in Figure 10. First, in this degradation process, the active substances (•OH, h^+ and $•O_2^-$) produced by the PEF reaction attack the methyl groups on the isoxazole ring in SMX, the C=C connecting methyl groups and the amine group sites on the aromatic ring. In pathway A, mainly •OH and the C=C on the isoxazole ring have an electrophilic addition reaction, forming dihydroxy-substituted SMX derivative P1 (m/z = 288). Further, the C–O bond on the isoxazole ring continues to be attacked by oxides, and isoxazole is ring-opened. The single bond oxime intermediate P2 (m/z = 246) is formed at the N–O bond position [84]. Oxime can dehydrate with molecular oxygen and release hydroxyl to form intermediate P3 (m/z = 198) [85]. The other pathway B mainly attacks the methyl group (-CH_3) on the isoxazole ring through $•O_2^-$, which leads to the oxidation reaction leading to the cleavage of the N–O bond position and the release of the methyl group at the same time. The intermediate P4 (m/z = 227) with an aldehyde group side chain can be formed through structural recombination [86]. Under acidic conditions, N=C was extremely unstable, and further oxidation of $•O_2^-$ would lead to the rupture of the N=C bond of the P4 side chain, resulting in intermediate P5 (m/z = 178). The hydroxylation of P5 resulted in the formation of hydroxy p-aminobenzene sulfonic acid P6 and P7 (m/z = 177, m/z = 192), which was consistent with previous reports by Liu and Chen et al. [87,88]. The third pathway C may be through holes and nucleophilic •OH attracting the electron-donating group amine group on the benzene ring, leading to the deamination reaction of aniline, releasing NH_4^+ and forming intermediate product P8 (m/z = 238) [89]. Then the addition reaction occurs, and the hydroxyl group rapidly replaces the para-hydrogen of the sulfonyl group to generate the

hydroxylated product P9 (m/z = 254). Furthermore, the S–N bond, as the electron-rich site of the intermediate P9, will also be attacked by h^+ and •OH, resulting in the rupture of the sulfonamide bond, forming hydroxy-p-hydroxybenzene sulfonic acid P10 (m/z = 174) and 3-amino-5- methylisoxazole P11 (m/z = 99). In addition, the coupling reaction in product P10 can also form azo compound P12 (m/z = 209) [90]. On the basis of the transformation of SMX by pathways A, B, and C, the strong oxidant •OH can further attack the amino, sulfonyl, benzene, and isoxazole rings on P3, P6-7, and P10-12.

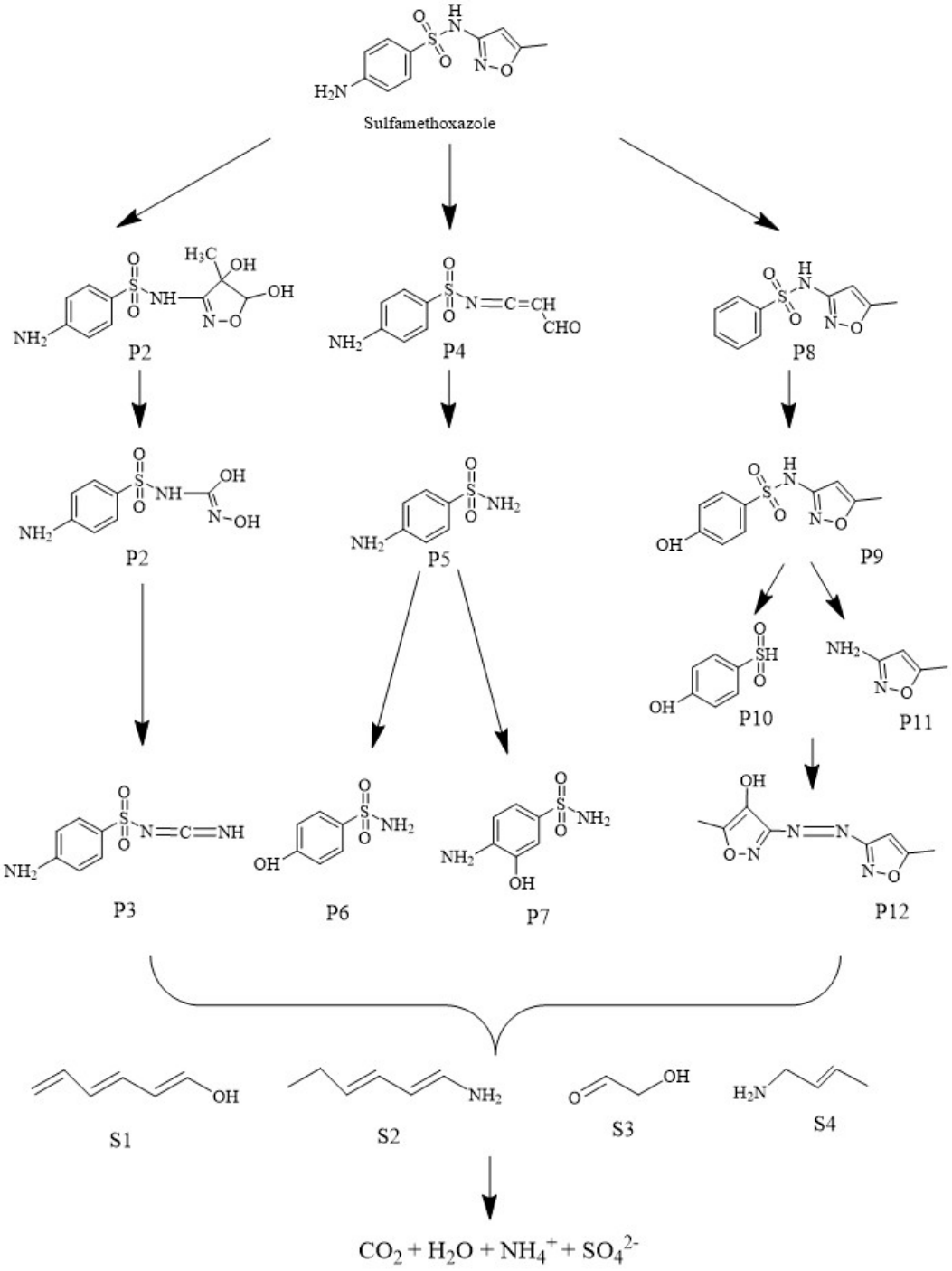

Figure 10. Proposed SMX degradation pathway in PEF process.

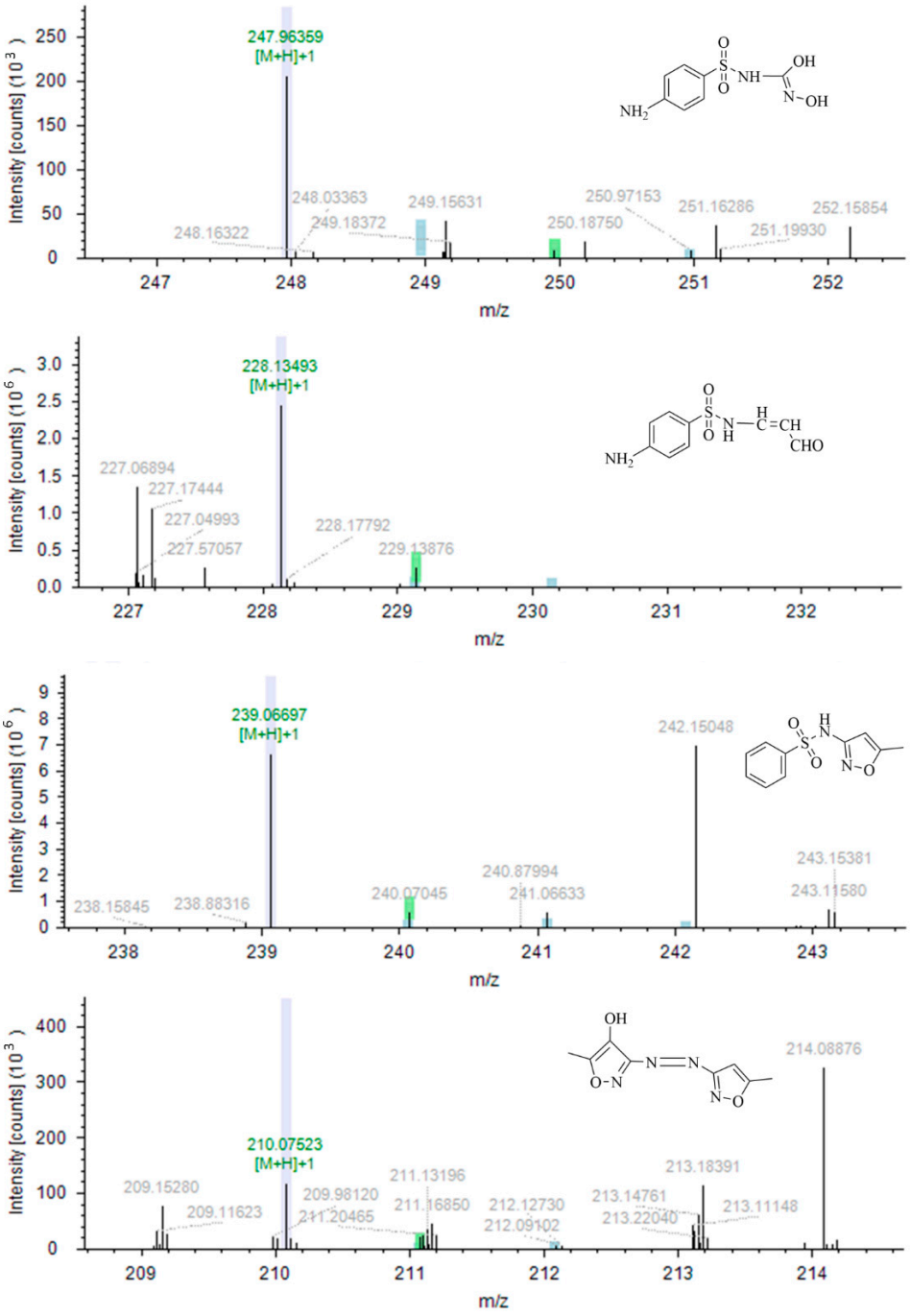

Figure 11. Intermediate product spectrum of SMX degradation.

According to the identified fragments, it can be inferred that the generated ring-opening products are small molecular compounds S1-4. It has also been proved in the studies of many scholars that these short-chain acids can be further oxidized into CO_2 and H_2O while SO_4^{2-} and NH_4^+ ions are released, leading to the complete mineralization of SMX [79,91,92].

Based on the above analysis, in the PEF process, MOF-525-Fe/Zr-modified cathode catalyzed by active free radicals selectively and non-selectively attack SMX sites, hydroxylation, oxidation, deamination, ring-opening, and bond cracking of SMX molecules will occur continuously, and intermediate products will continue to transform. Finally, complete degradation mineralization of SMX was achieved.

3. Materials and Methods

3.1. Materials and Reagents

Sulfamethoxazole (SMX), 4,4′,4′′,4′′′-(porphine-5,10,15,20-tetrayl) tetrakis (benzoic acid) (TCPP), sodium sulfate anhydrous (Na_2SO_4), zirconyl chloride octahydrate ($ZrOCl_2 \cdot 8H_2O$), N, N-dimethylformamide (DMF), and benzoic acid ($C_7H_6O_2$) were obtained from Aladdin (Shanghai, China). Potassium titanyl oxalate ($K_2TiO \cdot C_4O_8$) and salicylic acid (SA) were supplied by Macklin (Shanghai, China). Iron (II) sulfate hydrate ($FeSO_4 \cdot 7H_2O$), sulfuric acid (H_2SO_4), and acetone (C_3H_6O) were purchased from Guangdong Chemical Reagent Factory. Naphthol perfluorosulfonate solution (Nafion, 5 wt%) was purchased from Dupont Co., Ltd. of America (Wilmington, DE, USA). CF was purchased from Tianjin Carbon Plant. HPLC methanol and acetonitrile were purchased from Merch (Darmstadt, Germany). The water used to prepare the solution in this study is ultrapure water, and the purity of chemicals without special instructions is AR.

3.2. Preparation of MOF-525, MOF-525-Fe/Zr and Their Modified Cathodes

The MOF-525 is synthesized according to previous research reported by Yu et al. [28]. The preparation method of MOF-525-Fe/Zr and its modified cathode is as follows. First, benzoic acid and $ZrOCl_2 \cdot 8H_2O$ were weighed and dissolved in 6 mL DMF to obtain Zr-oxo SBUs precursor (phase A). Then TCPP and $FeSO_4 \cdot 7H_2O$ were weighed and dissolved in 6 mL DMF to obtain Fe-TCPP precursor (phase B). Then, phase A and phase B were mixed up and a solvent-thermal reaction was carried out at 100 °C for 2 h. After cooling down to room temperature, they were removed. Then mixed and mutually dissolved A and B phases were moved to a 100 mL reactor, the solvent-thermal reaction was carried out at 80 °C for 24 h, and after that placed at room temperature to cool down. Finally, the material was washed with DMF, acetone, and ethanol three times, and then dried in a vacuum for 12 h to obtain the electronic rearrangement of MOF-525 by metalloporphyrin ligand, namely MOF-525-Fe/Zr.

The purchased commercial CF was cleaned and activated on the surface. After drying, the CF was cut in accordance with the size ratio of 1 × 1.5 cm. About 12 mg MOF-525 or MOF-525-Fe/Zr powders were dissolved in 1 mL anhydrous ethanol and then dispersed well by ultrasound for 10 min. Then 30 µL Nafion was added. After another ultrasonic dispersion for 30 min, the mixture was spread on the pretreated CF evenly. MOF-525-modified cathode (named MOF-525@CF) and MOF-525-Fe/Zr-modified cathode (named MOF-525-Fe/Zr@CF) were obtained after natural drying.

3.3. Characterization and Performance Analysis Methods

A 5 kV field emission scanning electron microscope (FE-SEM), a high-angle annular dark field scanning transmission electron microscope (HAADF-TEM), and energy dispersive X-ray spectrometer (EDX) were employed to characterize the sample morphologies and element mapping. The pore structure and surface properties of the catalysts were analyzed by nitrogen adsorption and desorption isothermal curves (McAsap 2460, Atlanta, GA, USA). The structure and composition of MOF-525 and MOF-525-Fe/Zr were characterized by Raman excitation spectroscopy (Horiba company-LabRAM HR Evolution, Tokyo, Japan). Tafel slope and transient photocurrent were measured using an electrochemical workstation (Chenhua Instrument Company-CHI 760E, Shanghai, China) equipped with a platinum electrode counter electrode and saturated calomel electrode (SCE) as a reference electrode.

3.4. DFT Simulation Calculation Parameters

All computations were carried out by density functional theory using the B3LYP hybrid functional [93] with Grimme's dispersion correction of D3 version (Becke–Johnson damping) [94] implemented in the Gaussian 16 suite of programs [95]. Geometry optimizations of the TCPP and TCPP-Fe ligands were performed using the def2-SVP basis set [96,97] for all atoms. Analytical Hessians were computed with the same basis set to

determine the nature of the stationary points (zero imaginary frequencies for minima). The HOMO-LUMO energy calculations of two ligands and zirconium-oxygen clusters were performed on the optimized geometries and crystal structure respectively with the larger def2-QZVPP basis set [96,97] on all atoms. An effective core potential [97] associated with the ahlrichs family basis set was used on Zr. The cubes of HOMO and LUMO were generated by Multiwfn software [98] from the data in the corresponding formatted checkpoint files. The HOMOs and LUMOs were drawn using VMD 1.9.3 software (University of Illinois, Champaign, IL, USA) [99] with the isosurface value of 0.02 e/Å3.

3.5. The PEF Process Was Constructed to Degrade SMX

The PEF process was independently built in this study, and the reaction was carried out in a 150 mL electrolytic cell, which contains 100 mL solution, 10 mg/L SMX, and 0.1 mol/L Na_2SO_4. Using DC power supply, a platinum electrode (1.5 cm × 1 cm) and different catalyst-modified electrodes were used as anode and cathode, oxygen for the reaction was supplied by an air pump connected to an aerator pipe near the cathode at a flow rate of 1 mL/min. The UV lamp (the wavelength of 254 nm and the rated power in 10 w) was suspended above the electrolytic cell. Before the SMX degradation experiments, the pH of the solution was adjusted to 3.0 (0.1 mM·H_2SO_4 and NaOH solution are used) and the reflux current was set to 40 mA. During the reaction process, 1 mL of the degradation solution was removed at a certain interval and filtered in a 0.22 μm glass fiber membrane for the determination of the concentration of SMX. The degradation reaction lasted 180 min in total. The concentration of SMX was quantitatively analyzed by high-performance liquid chromatography (HPLC) (method parameter details are shown in Text S1). The degradation rate (R) of SMX degradation in the PEF process was calculated by Equation (9). Each group of degradation experiments was conducted three times and the average was taken as the final result.

$$R = \frac{C_0 - C}{C_0} \times 100\% \quad (9)$$

In the formula, C represents the concentration of SMX at time T (mg/L), and C_0 represents the initial concentration of SMX (mg/L). In this study, the change of Total Organic Carbon (TOC) in the reaction process was measured by the German element Vario TOC analyzer (Elementar Analysensysteme GmbH, Hanau, German), in order to evaluate the effect of the catalyst on the mineralization of organic matter.

In this study, inductively coupled plasma emission spectrometer (ICP-OES) was used to determine the leaching concentration of iron and zirconium ions in the solution after each reusability experiment. The potassium titanate colorimetric method was used to test H_2O_2 concentration in the process with different reaction time points (Text S2), and •OH concentration in solution was determined by the salicylic acid (SA) capture method (Text S2). The SMX intermediates were separated and tested by High-Performance Liquid Chromatography (Agilent Technologies inc-Agilent 1290 Series, Palo Alto, Santa Clara, CA, USA)/Tandem Mass Spectrometry (Bruker Daltonics Inc-Bruker Maxis impact, Billerica, MA, USA) (HPLC-MS).

4. Conclusions

In this study, a new electronic structure MOF-525-Fe/Zr was designed and assembled by pre-metallized porphyrin ligand which retained the characteristic structure and large specific surface area of MOF-525 and expanded the pore volume (0.37 cm^3/g), average pore size (3.68 nm). The multistage porous structure of microporous and mesoporous is beneficial to the rapid diffusion and reaction of active species. Furthermore, DFT calculated HOMO–LUMO energy gaps and electronic distribution revealed that the metalloporphyrin energy levels could effectively modify the electronic structure of MOF. d→π * electron transfer can occur in Fe-TCPP (MLCT), and π→π * electron orbital transfer can occur between Zr-oxo SBUs and Fe-TCPP structure (LCCT). After Zr-oxo SBUs coordinated with Fe-TCPP, these charge transitions co-stimulated by photoelectricity provide periodic

D-A electron conduction paths in MOF-525-Fe/Zr, which can improve the active species formation and transfer efficiency. Owing to their favorable pore and electronic structure as well as its stability, MOF-525-Fe/Zr shows great promise for the application in the catalytic process of PEF. •OH and h^+ generated from MOF-525-Fe/Zr-modified cathode-catalyzed PEF process will catalyze hydroxylation and other cracking reactions of SMX, and finally complete mineralization of SMX in the actual water environment.

Supplementary Materials: The following supporting information can be downloaded at: https://www.mdpi.com/article/10.3390/catal12060671/s1; Text S1: Method for SMX concentration; Text S2: Method for the concentration of H_2O_2 and •OH [100,101].

Author Contributions: Conceptualization, C.Q. and J.C.; methodology, C.Q.; software, J.L.; validation, K.D., Y.C. and Y.H.; formal analysis, S.H.; investigation, C.Q.; resources, J.C.; data curation, C.Q.; writing, C.Q.; visualization, C.Q. and S.H. All authors have read and agreed to the published version of the manuscript.

Funding: This research was funded by National Natural Science Foundation of China (No. 21976060), Dongguan Science and Technology project (No. 2020101117019) and Introduced innovative R&D team leadership of Dongguan city (No. 2020607263005).

Data Availability Statement: All the relevant data used in this study have been provided in the form of figures and tables in the published article, and all data provided in the present manuscript are available to whom it may concern.

Acknowledgments: The authors would like to thank Zhenyun Huang from Shiyanjia Lab (www.shiyanjia.com (accessed on 1 July 2021)) for the Raman analysis.

Conflicts of Interest: The authors declare no conflict of interest.

References

1. Liu, Y.; Zhao, Y.; Wang, J. Fenton/Fenton-like processes with in-situ production of hydrogen peroxide/hydroxyl radical for degradation of emerging contaminants: Advances and prospects. *J. Hazard. Mater.* **2021**, *404*, 124191. [CrossRef] [PubMed]
2. Ziembowicz, S.; Kida, M. Limitations and future directions of application of the Fenton-like process in micropollutants degradation in water and wastewater treatment: A critical review. *Chemosphere* **2022**, *296*, 134041. [CrossRef] [PubMed]
3. Su, Z.; Li, J.; Zhang, D.; Ye, P.; Li, H.; Yan, Y. Novel flexible Fenton-like catalyst: Unique CuO nanowires arrays on copper mesh with high efficiency across a wide pH range. *Sci. Total Environ.* **2019**, *647*, 587–596. [CrossRef]
4. Song, G.; Du, X.; Zheng, Y.; Su, P.; Tang, Y.; Zhou, M. A novel electro-Fenton process coupled with sulfite: Enhanced Fe^{3+} reduction and TOC removal. *J. Hazard. Mater.* **2022**, *422*, 126888. [CrossRef] [PubMed]
5. Hu, T.; Deng, F.; Feng, H.; Zhang, J.; Shao, B.; Feng, C.; Tang, W.; Tang, L. Fe/Co bimetallic nanoparticles embedded in MOF-derived nitrogen-doped porous carbon rods as efficient heterogeneous electro-Fenton catalysts for degradation of organic pollutants. *Appl. Mater. Today* **2021**, *24*, 101161. [CrossRef]
6. Devi, L.G.; Raju, K.A.; Kumar, S.G.; Rajashekhar, K.E. Photo-degradation of di azo dye Bismarck Brown by advanced photo-Fenton process: Influence of inorganic anions and evaluation of recycling efficiency of iron powder. *J. Taiwan Inst. Chem. Eng.* **2011**, *42*, 341–349. [CrossRef]
7. Giannakis, S.; López, M.I.P.; Spuhler, D.; Pérez, J.A.S.; Ibáñez, P.F.; Pulgarin, C. Solar disinfection is an augmentable, in situ-generated photo-Fenton reaction—Part 1: A review of the mechanisms and the fundamental aspects of the process. *Appl. Catal. B* **2016**, *199*, 199–223. [CrossRef]
8. Ganiyu, S.O.; Zhou, M.; Martinez-Huitle, C.A. Heterogeneous electro-Fenton and photoelectro-Fenton processes: A critical review of fundamental principles and application for water/wastewater treatment. *Appl. Catal. B* **2018**, *235*, 103–129. [CrossRef]
9. Brillas, E. Recent development of electrochemical advanced oxidation of herbicides. A review on its application to wastewater treatment and soil remediation. *J. Clean. Prod.* **2021**, *290*, 125841. [CrossRef]
10. Zhao, H.; Ying, C.; Peng, Q.; Wang, Q.; Zhao, G. Catalytic activity of MOF(2Fe/Co)/carbon aerogel for improving H_2O_2 and OH generation in solar photo-electro-Fenton process. *Appl. Catal. B* **2017**, *203*, 127–137. [CrossRef]
11. Bai, X.; Li, Y.; Xie, L.; Liu, X.; Zhan, S.; Hu, W. A novel Fe-free photo-electro-Fenton-like system for enhanced ciprofloxacin degradation: Bifunctional Z-scheme WO_3/g-C_3N_4. *Environ. Sci. Nano* **2019**, *6*, 2850–2862. [CrossRef]
12. Ye, Z.; Schukraft, G.E.M.; L'Hermitte, A.; Xiong, Y.; Brillas, E.; Petit, C.; Sires, I. Mechanism and stability of an Fe-based 2D MOF during the photoelectro-Fenton treatment of organic micropollutants under UVA and visible light irradiation. *Water Res.* **2020**, *184*, 115986. [CrossRef] [PubMed]
13. Thomas, N.; Dionysiou, D.D.; Pillai, S.C. Heterogeneous Fenton catalysts: A review of recent advances. *J. Hazard. Mater.* **2021**, *404*, 124082. [CrossRef] [PubMed]

14. Brillas, E. A review on the photoelectro-Fenton process as efficient electrochemical advanced oxidation for wastewater remediation. Treatment with UV light, sunlight, and coupling with conventional and other photo-assisted advanced technologies. *Chemosphere* **2020**, *250*, 126198. [CrossRef]
15. Alduhaish, O.M.; Shaik, M.R.; Adil, S.F. Photo-Induced Preparation of Ag@MOF-801 Composite Based Heterogeneous Nanocatalyst for the Production of Biodiesel. *Catalysts* **2022**, *12*, 533. [CrossRef]
16. Cheng, M.; Lai, C.; Liu, Y.; Zeng, G.; Huang, D.; Zhang, C.; Qin, L.; Hu, L.; Zhou, C.; Xiong, W. Metal-organic frameworks for highly efficient heterogeneous Fenton-like catalysis. *Coord. Chem. Rev.* **2018**, *368*, 80–92. [CrossRef]
17. Du, C.; Zhang, Y.; Zhang, Z.; Zhou, L.; Yu, G.; Wen, X.; Chi, T.; Wang, G.; Su, Y.; Deng, F. Fe-based metal organic frameworks (Fe-MOFs) for organic pollutants removal via photo-Fenton: A review. *Chem. Eng. J.* **2022**, *431*, 133932. [CrossRef]
18. Hu, T.; Tang, L.; Feng, H.; Zhang, J.; Li, X.; Zuo, Y.; Lu, Z.; Tang, W. Metal-organic frameworks (MOFs) and their derivatives as emerging catalysts for electro-Fenton process in water purification. *Coord. Chem. Rev.* **2022**, *451*, 214277. [CrossRef]
19. Herrera-Herrera, P.A.; Rodriguez-Sevilla, E.; Varela, A.S. The role of the metal center on charge transport rate in MOF-525: Cobalt and nickel porphyrin. *Dalton Trans.* **2021**, *50*, 16939–16944. [CrossRef]
20. Shayegan, H.; Ali, G.A.; Safarifard, V. Recent progress in the removal of heavy metal ions from water using metal-organic frameworks. *ChemistrySelect* **2020**, *5*, 124–146. [CrossRef]
21. Song, Z.; Cheng, N.; Lushington, A.; Sun, X. Recent Progress on MOF-Derived Nanomaterials as Advanced Electrocatalysts in Fuel Cells. *Catalysts* **2016**, *6*, 116. [CrossRef]
22. Paulus, B.C.; Adelman, S.L.; Jamula, L.L.; McCusker, J.K. Leveraging excited-state coherence for synthetic control of ultrafast dynamics. *Nature* **2020**, *582*, 214–218. [CrossRef] [PubMed]
23. Wang, Z.; Wang, B.; Yang, Y.; Cui, Y.; Wang, Z.; Chen, B.; Qian, G. Mixed-metal-organic framework with effective Lewis acidic sites for sulfur confinement in high-performance lithium-sulfur batteries. *ACS Appl. Mater. Interfaces* **2015**, *7*, 20999–21004. [CrossRef] [PubMed]
24. Lee, Y.; Kim, S.; Kang, J.K.; Cohen, S.M. Photocatalytic CO_2 reduction by a mixed metal (Zr/Ti), mixed ligand metal-organic framework under visible light irradiation. *Chem. Commun.* **2015**, *51*, 5735–5738. [CrossRef]
25. Chen, X.; Lei, L.; Liu, S.; Han, J.; Li, R.; Men, J.; Li, L.; Wei, L.; Sheng, Y.; Yang, L.; et al. Occurrence and risk assessment of pharmaceuticals and personal care products (PPCPs) against COVID-19 in lakes and WWTP-river-estuary system in Wuhan, China. *Sci. Total Environ.* **2021**, *792*, 148352. [CrossRef]
26. Wang, D.; Sui, Q.; Zhao, W.T.; Lv, S.; Qiu, Z.F.; Yu, G. Research progress of pharmaceutical and personal care products in the Surface water environment of China. *Chin. Sci. Bull.* **2014**, *59*, 743–751.
27. Kairigo, P.; Ngumba, E.; Sundberg, L.-R.; Gachanja, A.; Tuhkanen, T. Occurrence of antibiotics and risk of antibiotic resistance evolution in selected Kenyan wastewaters, surface waters and sediments. *Sci. Total Environ.* **2020**, *720*, 137580. [CrossRef]
28. Yu, K.; Ahmed, I.; Won, D.-I.; Lee, W.I.; Ahn, W.-S. Highly efficient adsorptive removal of sulfamethoxazole from aqueous solutions by porphyrinic MOF-525 and MOF-545. *Chemosphere* **2020**, *250*, 126133. [CrossRef]
29. Adil, H.I.; Thalji, M.R.; Yasin, S.A.; Saeed, I.A.; Assiri, M.A.; Chong, K.F.; Ali, G.A. Metal-organic frameworks (MOFs) based nanofiber architectures for the removal of heavy metal ions. *RSC Adv.* **2022**, *12*, 1433–1450. [CrossRef]
30. Luo, E.; Chu, Y.; Liu, J.; Shi, Z.; Zhu, S.; Gong, L.; Ge, J.; Choi, C.H.; Liu, C.; Xing, W. Pyrolyzed M–N_x catalysts for oxygen reduction reaction: Progress and prospects. *Energy Environ. Sci.* **2021**, *14*, 2158–2185. [CrossRef]
31. Chung, H.T.; Cullen, D.A.; Higgins, D.; Sneed, B.T.; Holby, E.F.; More, K.L.; Zelenay, P. Direct atomic-level insight into the active sites of a high-performance PGM-free ORR catalyst. *Science* **2017**, *357*, 479–484. [CrossRef] [PubMed]
32. Zhou, X.; Xu, D.; Chen, Y.; Hu, Y. Enhanced degradation of triclosan in heterogeneous E-Fenton process with MOF-derived hierarchical Mn/Fe@PC modified cathode. *Chem. Eng. J.* **2020**, *384*, 123324. [CrossRef]
33. Jaroniec, M.; Choma, J.; Kruk, M. Assessment of reliability of the Horvath-Kawazoe pore size analysis method using argon adsorption isotherms on ordered mesoporous silicas. *Colloids Surf. A-Physicochem. Eng. Asp.* **2003**, *214*, 263–269. [CrossRef]
34. Tao, Y.; Li, R.; Zhu, H.; Li, Z. Ceria nanoparticles uniformly decorated on graphene nanosheets with coral-like morphology for high-performance supercapacitors. *Mater. Res. Bull.* **2016**, *78*, 163–171. [CrossRef]
35. Zhao, L.; Guanhua, N.; Lulu, S.; Qian, S.; Shang, L.; Kai, D.; Jingna, X.; Gang, W. Effect of ionic liquid treatment on pore structure and fractal characteristics of low rank coal. *Fuel* **2020**, *262*, 116513. [CrossRef]
36. Byeon, A.; Lee, K.J.; Lee, M.J.; Lee, J.S.; Lee, I.H.; Park, H.-Y.; Lee, S.Y.; Yoo, S.J.; Jang, J.H.; Kim, H.-J. Effect of Catalyst Pore Size on the Performance of Non-Precious Fe/N/C-Based Electrocatalysts for High-Temperature Polymer Electrolyte Membrane Fuel Cells. *ChemElectroChem* **2018**, *5*, 1805–1810. [CrossRef]
37. Galarneau, A.; Mehlhorn, D.; Guenneau, F.; Coasne, B.; Villemot, F.; Minoux, D.; Aquino, C.; Dath, J.-P. Specific surface area determination for microporous/mesoporous materials: The case of mesoporous FAU-Y zeolites. *Langmuir* **2018**, *34*, 14134–14142. [CrossRef]
38. Chen, T.; Wang, F.; Cao, S.; Bai, Y.; Zheng, S.; Li, W.; Zhang, S.; Hu, S.-X.; Pang, H. In-situ Synthesis of MOF-74 Family for High Areal Energy Density of Aqueous Nickel-Zinc Batteries. *Adv. Mater.* **2022**, 2201779. [CrossRef]
39. Han, L.; Liu, X.; Zhang, X.; Li, M.; Li, D.; Qin, P.; Tian, S.; Lu, M.; Cai, Z. Preparation of multivariate zirconia metal-organic frameworks for highly efficient adsorption of endocrine disrupting compounds. *J. Hazard. Mater.* **2022**, *424*, 127559. [CrossRef]
40. Feng, D.; Chung, W.-C.; Wei, Z.; Gu, Z.-Y.; Jiang, H.-L.; Chen, Y.-P.; Darensbourg, D.J.; Zhou, H.-C. Construction of Ultrastable Porphyrin Zr Metal-Organic Frameworks through Linker Elimination. *J. Am. Chem. Soc.* **2013**, *135*, 17105–17110. [CrossRef]

41. Xu, W.; Ding, Q.; Sang, P.; Xu, J.; Guo, W. The Effect of Modified Metal Center in Ligand for CO_2 Capture in Novel Zr-Based Porphyrinic Metal-Organic Frameworks:A Computational Investigation. *J. Phys. Chem. C* **2015**, *119*, 150903151317006. [CrossRef]
42. Usov, P.M.; Leong, C.F.; Chan, B.; Hayashi, M.; Kitagawa, H.; Sutton, J.J.; Gordon, K.C.; Hod, I.; Farha, O.K.; Hupp, J.T.; et al. Probing charge transfer characteristics in a donor-acceptor metal-organic framework by Raman spectroelectrochemistry and pressure-dependence studies. *Phys. Chem. Chem. Phys.* **2018**, *20*, 25772–25779. [CrossRef] [PubMed]
43. Ma, G.; Chen, H.; Zhang, Q.; Ma, J.; Yu, Q.; Han, L.; Chen, C.; Song, R. Protective characterization of low dose sodium nitrite on yak meat myoglobin in a hydroxy radical oxidation environment: Fourier Transform Infrared spectroscopy and laser Micro-Raman spectroscopy. *LWT Food Sci. Technol.* **2019**, *116*, 108556. [CrossRef]
44. Liu, Y.-C. Characteristics of vibration modes of polypyrrole on surface-enhanced Raman scattering spectra. *J. Electroanal. Chem.* **2004**, *571*, 255–264. [CrossRef]
45. Yan, C.; Jin, J.; Wang, J.; Zhang, F.; Tian, Y.; Liu, C.; Zhang, F.; Cao, L.; Zhou, Y.; Han, Q. Metal-organic frameworks (MOFs) for the efficient removal of contaminants from water: Underlying mechanisms, recent advances, challenges, and future prospects. *Coord. Chem. Rev.* **2022**, *468*, 214595. [CrossRef]
46. Roy, D.R.; Shah, E.V.; Roy, S.M. Optical activity of Co-porphyrin in the light of IR and Raman spectroscopy: A critical DFT investigation. *Spectrochim. Acta Part A* **2018**, *190*, 121–128. [CrossRef]
47. Thirunavukkarasu, K.; Rajkumar, P.; Selvaraj, S.; Gunasekaran, S.; Kumaresan, S. Electronic structure, vibrational (FT-IR and FT-Raman), UV-Vis and NMR analysis of 5-(4-(2-(5-ethylpyridin-2-yl) ethoxy) benzyl) thiazolidine-2,4-dione by quantum chemical method—ScienceDirect. *Chem. Data Collect.* **2018**, *17–18*, 263–275. [CrossRef]
48. Wu, M.; Zhang, Y.; Xiang, M. Structural, Raman spectroscopic and microwave dielectric studies on $(1-x)$ $NiZrNb_2O_8 - x$ $ZnTa_2O_6$. *J. Mater. Sci.-Mater. Electron.* **2018**, *29*, 14471–14478. [CrossRef]
49. Zhao, C.-X.; Li, B.-Q.; Liu, J.-N.; Zhang, Q. Intrinsic Electrocatalytic Activity Regulation of M-N-C Single-Atom Catalysts for the Oxygen Reduction Reaction. *Angew. Chem. Int. Ed.* **2021**, *60*, 4448–4463. [CrossRef]
50. Zhang, S.; Xu, W.; He, P.; Chen, X.; Su, L.; Ma, T.; Lu, Z. Tafel Analysis Guided Optimization of ZnNP-OC Catalysts for the Selective 2-Electron Oxygen Reduction Reaction in Neutral Media. *J. Phys. Chem. Lett.* **2022**, *13*, 3409–3416. [CrossRef]
51. Ding, D.; Shen, K.; Chen, X.; Chen, H.; Chen, J.; Fan, T.; Wu, R.; Li, Y. Multi-Level Architecture Optimization of MOF-Templated Co-Based Nanoparticles Embedded in Hollow N-Doped Carbon Polyhedra for Efficient OER and ORR. *ACS Catal.* **2018**, *8*, 7879–7888. [CrossRef]
52. Shah, S.S.A.; Najam, T.; Molochas, C.; Nazir, M.A.; Brouzgou, A.; Javed, M.S.; Rehman, A.U.; Tsiakaras, P. Nanostructure Engineering of Metal-Organic Derived Frameworks: Cobalt Phosphide Embedded in Carbon Nanotubes as an Efficient ORR Catalyst. *Molecules* **2021**, *26*, 6672. [CrossRef] [PubMed]
53. Zhao, C.-X.; Li, B.-Q.; Liu, J.-N.; Huang, J.-Q.; Zhang, Q. Transition metal coordinated framework porphyrin for electrocatalytic oxygen reduction. *Chin. Chem. Lett.* **2019**, *30*, 911–914. [CrossRef]
54. Gao, C.; Low, J.; Long, R.; Kong, T.; Zhu, J.; Xiong, Y. Heterogeneous Single-Atom Photocatalysts: Fundamentals and Applications. *Chem. Rev.* **2020**, *120*, 12175–12216. [CrossRef]
55. Yu, F.; Cao, T.Y.; Ma, H.; Yang, J.; Jing, L. Enhancing the yield of H_2O_2 and bisphenol A degradation via a synergistic effect of photoelectric co-catalysis by using NPC/C_3N_4 electrode. *Int. J. Hydrogen Energy* **2022**, *47*, 16873–16886. [CrossRef]
56. Li, D.; Hua, T.; Li, X.; Cheng, J.; Du, K.; Hu, Y.; Chen, Y. In-situ fabrication of ionic liquids/MIL-68(In)-NH_2 photocatalyst for improving visible-light photocatalytic degradation of doxycycline hydrochloride. *Chemosphere* **2022**, *292*, 133461. [CrossRef]
57. Han, J.; Zhu, Z.; Li, N.; Chen, D.; Lu, J. Metalloporphyrin-based D-A Type Conjugated Organic Polymer Nanotube for Efficient Photocatalytic Degradation. *Appl. Catal. B* **2021**, *291*, 120108. [CrossRef]
58. Li, W.-Q.; Wang, Y.-X.; Chen, J.-Q.; Hou, N.-N.; Li, Y.-M.; Liu, X.-C.; Ding, R.-R.; Zhou, G.-N.; Li, Q.; Zhou, X.-G.; et al. Boosting photo-Fenton process enabled by ligand-to-cluster charge transfer excitations in iron-based metal organic framework. *Appl. Catal. B* **2022**, *302*, 120882. [CrossRef]
59. Shah, S.S.A.; Najam, T.; Wen, M.; Zang, S.-Q.; Waseem, A.; Jiang, H.-L. Metal-Organic Framework-Based Electrocatalysts for CO_2 Reduction. *Small Struct.* **2022**, *3*, 2100090. [CrossRef]
60. Avilov, I.; Minoofar, P.; Cornil, J.; De Cola, L. Influence of substituents on the energy and nature of the lowest excited states of heteroleptic phosphorescent Ir(III) complexes: A joint theoretical and experimental study. *J. Am. Chem. Soc.* **2007**, *129*, 8247–8258. [CrossRef]
61. Zhao, N.; Wu, Y.-H.; Wen, H.-M.; Zhang, X.; Chen, Z.-N. Conversion from ILCT to LLCT/MLCT Excited State by Heavy Metal Ion Binding in Iridium(III) Complexes with Functionalized 2,2′-Bipyridyl Ligands. *Organometallics* **2009**, *28*, 5603–5611. [CrossRef]
62. Shahroosvand, H.; Zakavi, S.; Sousaraei, A.; Eskandari, M. Saddle-shaped porphyrins for dye-sensitized solar cells: New insight into the relationship between nonplanarity and photovoltaic properties. *Pccp* **2015**, *17*, 6347–6358. [CrossRef] [PubMed]
63. Mayorga, B.L.; Sandoval-Chávez, C.; Carreon-Castro, M.; Ugalde-Saldívar, V.; Cortes-Guzman, F.; López-Cortés, J.; Ortega-Alfaro, M.C. Ferrocene amphiphilic D–π–A dyes: Synthesis, redox behavior and determination of band gaps. *New J. Chem.* **2018**, *42*, 6101–6113. [CrossRef]
64. Chen, L.; Luque, R.; Li, Y. Controllable design of tunable nanostructures inside metal-organic frameworks. *Chem. Soc. Rev.* **2017**, *46*, 4614–4630. [CrossRef]
65. Zhang, M.-H.; Dong, H.; Zhao, L.; Wang, D.-X.; Meng, D. A review on Fenton process for organic wastewater treatment based on optimization perspective. *Sci. Total Environ.* **2019**, *670*, 110–121. [CrossRef]

66. Xu, X.-Y.; Chu, C.; Fu, H.; Du, X.-D.; Wang, P.; Zheng, W.; Wang, C.-C. Light-responsive UiO-66-NH_2/Ag_3PO_4 MOF-nanoparticle composites for the capture and release of sulfamethoxazole. *Chem. Eng. J.* **2018**, *350*, 436–444. [CrossRef]
67. Ye, Z.; Guelfi, D.R.V.; Álvarez, G.; Alcaide, F.; Brillas, E.; Sirés, I. Enhanced electrocatalytic production of H_2O_2 at Co-based air-diffusion cathodes for the photoelectro-Fenton treatment of bronopol. *Appl. Catal. B* **2019**, *247*, 191–199. [CrossRef]
68. Li, S.; Hua, T.; Yuan, C.-S.; Li, B.; Zhu, X.; Li, F. Degradation pathways, microbial community and electricity properties analysis of antibiotic sulfamethoxazole by bio-electro-Fenton system. *Bioresour. Technol.* **2020**, *298*, 122501. [CrossRef]
69. Li, S.; Zhu, X.; Yu, H.; Wang, X.; Liu, X.; Yang, H.; Li, F.; Zhou, Q. Simultaneous sulfamethoxazole degradation with electricity generation by microbial fuel cells using Ni-MOF-74 as cathode catalysts and quantification of antibiotic resistance genes. *Environ. Res.* **2021**, *197*, 111054. [CrossRef]
70. Pu, M.; Wan, J.; Zhang, F.; Brusseau, M.L.; Ye, D.; Niu, J. Insight into degradation mechanism of sulfamethoxazole by metal-organic framework derived novel magnetic Fe@ C composite activated persulfate. *J. Hazard. Mater.* **2021**, *414*, 125598. [CrossRef]
71. Hang, J.; Yi, X.-H.; Wang, C.-C.; Fu, H.; Wang, P.; Zhao, Y. Heterogeneous photo-Fenton degradation toward sulfonamide matrix over magnetic Fe3S4 derived from MIL-100 (Fe). *J. Hazard. Mater.* **2022**, *424*, 127415. [CrossRef] [PubMed]
72. Ortega-Moreno, G.A.; Ayala-Durán, S.C.; Barbero, B.P.; Narda, G.E.; Bernini, M.C.; Nogueira, R.F.P. Photo-Fenton degradation of sulfamethoxazole using MIL-53 (Fe) under UVA LED irradiation and natural sunlight. *J. Environ. Chem. Eng.* **2022**, *10*, 107678. [CrossRef]
73. Wang, A.; Ni, J.; Wang, W.; Wang, X.; Liu, D.; Zhu, Q. MOF-derived N-doped ZnO carbon skeleton@ hierarchical Bi_2MoO_6 S-scheme heterojunction for photodegradation of SMX: Mechanism, pathways and DFT calculation. *J. Hazard. Mater.* **2022**, *426*, 128106. [CrossRef] [PubMed]
74. Zou, Y.; Qi, H.; Sun, Z. In-situ catalytic degradation of sulfamethoxazole with efficient CuCo–O@ CNTs/NF cathode in a neutral electro-Fenton-like system. *Chemosphere* **2022**, *296*, 134072. [CrossRef] [PubMed]
75. Saber, A.L.; Hameed, A.M.; Sayqal, A.A.; Alessa, H.; Alharbi, A. Iron-selective Poly (Vinyl Chloride) Membrane Electrode Based on Norfloxacin as a Neutral Carrier. *Int. J. Electrochem. Sci.* **2018**, *13*, 10076–10087. [CrossRef]
76. Pacheco-Álvarez, M.; Benítez, R.P.; Rodríguez-Narváez, O.M.; Brillas, E.; Peralta-Hernández, J.M. A critical review on paracetamol removal from different aqueous matrices by Fenton and Fenton-based processes, and their combined methods. *Chemosphere* **2022**, *303*, 134883. [CrossRef]
77. Yang, F.; Du, M.; Yin, K.; Qiu, Z.; Zhao, J.; Liu, C.; Zhang, G.; Gao, Y.; Pang, H. Applications of Metal-Organic Frameworks in Water Treatment: A Review. *Small* **2022**, *18*, 2105715. [CrossRef]
78. Chen, J.; Zhu, Y.; Kaskel, S. Porphyrin-Based Metal-Organic Frameworks for Biomedical Applications. *Angew. Chem. Int. Ed.* **2021**, *60*, 5010–5035. [CrossRef]
79. Wang, A.; Li, Y.-Y.; Estrada, A.L. Mineralization of antibiotic sulfamethoxazole by photoelectro-Fenton treatment using activated carbon fiber cathode and under UVA irradiation. *Appl. Catal. B* **2011**, *102*, 378–386. [CrossRef]
80. Zhang, Y.; Gao, M.; Wang, S.-G.; Zhou, W.; Sang, Y.; Wang, X.-H. Integrated electro-Fenton process enabled by a rotating Fe_3O_4/gas diffusion cathode for simultaneous generation and activation of H_2O_2. *Electrochim. Acta* **2017**, *231*, 694–704. [CrossRef]
81. Xu, P.; Xu, H.; Zheng, D. The efficiency and mechanism in a novel electro-Fenton process assisted by anodic photocatalysis on advanced treatment of coal gasification wastewater. *Chem. Eng. J.* **2019**, *361*, 968–974. [CrossRef]
82. Alcaide, F.; Alvarez, G.; Guelfi, D.R.V.; Brillas, E.; Sires, I. A stable CoSP/MWCNTs air-diffusion cathode for the photoelectro-Fenton degradation of organic pollutants at pre-pilot scale. *Chem. Eng. J.* **2020**, *379*, 122417. [CrossRef]
83. Xuan, S.N.; Zhang, G.; Yang, X. Mesocrystalline Zn-Doped Fe_3O_4 Hollow Submicrospheres: Formation Mechanism and Enhanced Photo-Fenton Catalytic Performance. *ACS Appl. Mater. Interfaces* **2017**, *9*, 8900.
84. Peng, Y.; Tong, W.; Xie, Y.; Hu, W.; Wang, Y. Yeast biomass-induced Co2P/biochar composite for sulfonamide antibiotics degradation through peroxymonosulfate activation. *Environ. Pollut.* **2020**, *268*, 115930. [CrossRef]
85. Yan, P.; Sui, Q.; Lyu, S.; Hao, H.; Schroder, H.F.; Gebhardt, W. Elucidation of the oxidation mechanisms and pathways of sulfamethoxazole degradation under Fe(II) activated percarbonate treatment. *Sci. Total Environ.* **2018**, *640*, 973–980. [CrossRef] [PubMed]
86. Guan, C.; Jiang, J.; Pang, S.; Ma, J.; Chen, X.; Lim, T.-T. Nonradical transformation of sulfamethoxazole by carbon nanotube activated peroxydisulfate: Kinetics, mechanism and product toxicity. *Chem. Eng. J.* **2019**, *378*, 122147. [CrossRef]
87. Liu, G.; Zhang, Z.; Lv, M.; Wang, H.; Chen, D.; Feng, Y. Photodegradation performance and transformation mechanisms of sulfamethoxazole by porous g-C_3N_4 modified with ammonia bicarbonate—ScienceDirect. *Sep. Purif. Technol.* **2020**, *235*, 116172. [CrossRef]
88. Chen, M.; Guo, C.; Hou, S.; Wu, L.; Lv, J.; Hu, C.; Zhang, Y.; Xu, J. In-situ fabrication of Ag/Pg-C_3N_4 composites with enhanced photocatalytic activity for sulfamethoxazole degradation. *J. Hazard. Mater.* **2019**, *366*, 219–228. [CrossRef]
89. Song, Y.; Huang, L.; Zhang, X.; Zhang, H.; Liu, Y. Synergistic Effect of Persulfate and g-C_3N_4 under Simulated Solar Light Irradiation: Implication for the Degradation of Sulfamethoxazole. *J. Hazard. Mater.* **2020**, *393*, 122379. [CrossRef]
90. Fu, J.; Feng, L.; Liu, Y.; Zhang, L.; Li, S. Electrochemical activation of peroxymonosulfate (PMS) by carbon cloth anode for sulfamethoxazole degradation. *Chemosphere* **2022**, *287*, 132094. [CrossRef]
91. Yong, L.; Qin, F.; Wang, J. Zn-Fe-CNTs catalytic in situ generation of H_2O_2 for Fenton-like degradation of sulfamethoxazole. *J. Hazard. Mater.* **2017**, *342*, 166.

92. Wang, Y.; Zhou, C.; Wu, J.; Niu, J. Insights into the electrochemical degradation of sulfamethoxazole and its metabolite by Ti/SnO_2-Sb/Er-PbO_2 anode. *Chin. Chem. Lett.* **2020**, *31*, 2673–2677. [CrossRef]
93. Stephens, P.J.; Devlin, F.J.; Chabalowski, C.F.; Frisch, M.J. Ab initio calculation of vibrational absorption and circular dichroism spectra using density functional force fields. *J. Phys. Chem.* **1994**, *98*, 11623–11627. [CrossRef]
94. Grimme, S.; Ehrlich, S.; Goerigk, L. Effect of the damping function in dispersion corrected density functional theory. *J. Comput. Chem.* **2011**, *32*, 1456–1465. [CrossRef] [PubMed]
95. Steinert, H.; Schwarz, C.; Kroll, A.; Gessner, V.H. Towards the preparation of stable cyclic amino (ylide) carbenes. *Molecules* **2020**, *25*, 796. [CrossRef]
96. Weigend, F.; Ahlrichs, R. Balanced basis sets of split valence, triple zeta valence and quadruple zeta valence quality for H to Rn: Design and assessment of accuracy. *Phys. Chem. Chem. Phys.* **2005**, *7*, 3297–3305. [CrossRef]
97. Weigend, F. Accurate Coulomb-fitting basis sets for H to Rn. *Phys. Chem. Chem. Phys.* **2006**, *8*, 1057–1065. [CrossRef]
98. Lu, T.; Chen, F. Multiwfn: A multifunctional wavefunction analyzer. *J. Comput. Chem.* **2012**, *33*, 580–592. [CrossRef]
99. Humphrey, W.; Dalke, A.; Schulten, K. VMD: Visual molecular dynamics. *J. Mol. Graph.* **1996**, *14*, 33–38. [CrossRef]
100. Liang, Z.Z.; Wang, H.Y.; Zheng, H.Q.; Zhang, W.; Cao, R. Porphyrin-based frameworks for oxygen electrocatalysis and catalytic reduction of carbon dioxide. *Chem. Soc. Rev.* **2021**, *50*, 2540–2581. [CrossRef]
101. Wang, C.; Niu, J.F.; Yin, L.F.; Huang, J.X.; Hou, L.A. Electrochemical degradation of fluoxetine on nanotube array intercalated anode with enhanced electronic transport and hydroxyl radical production. *Chem. Eng. J.* **2018**, *346*, 662–671. [CrossRef]